

Article

Controlled Two-Step Formation of Faceted Perovskite Rare-Earth Scandate Nanoparticles

Ryan J. Paull ¹, Tiffany Ly ¹, Zachary R. Mansley ¹, Kenneth R. Poeppelmeier ² and Laurence D. Marks ^{1,*}

¹ Department of Materials Science and Engineering, Northwestern University, Evanston, IL 60208, USA; rjpaul@u.northwestern.edu (R.J.P.); tiffanyly2015@u.northwestern.edu (T.L.); zacharymansley2021@u.northwestern.edu (Z.R.M.)

² Department of Chemistry, Northwestern University, Evanston, IL 60208, USA; krp@northwestern.edu

* Correspondence: l-marks@northwestern.edu

Received: 8 March 2019; Accepted: 19 April 2019; Published: 23 April 2019



Abstract: A general approach to the formation of well-faceted nanoparticles is discussed and successfully applied to the production of several rare-earth scandates. Two steps were used, with higher temperatures first to nucleate the perovskite phase, followed by lower temperatures to smooth the particle surfaces. Exploiting these two different regimes led to smaller nanoparticles with more faceting. This general approach may be tailored to other material systems as a step towards producing shape-controlled nanoparticles for a desired application.

Keywords: rare-earth scandate; perovskite; nucleation and growth

1. Introduction

Nanoparticles are used in an impressive number of applications, such as heterogeneous catalysis [1], plasmonics [2], cosmetics [3], reinforcing agents in advanced metals [4], and drug delivery [5], to name only a few. Nanomaterials containing rare-earth elements have particular functionality in biomedical applications and luminescence because of their low toxicity, chemical stability, and unique *f*-electrons [6,7]. The size of a particle can affect its electronic properties [8,9], optical properties [10,11], and coupled phenomena such as ferroelectricity [12,13]. In some cases, the size may also alter which phase is formed, which can change the properties altogether [14]. Nanoparticle surfaces play an important role in dictating the overall properties with decreasing size. Different surfaces exhibit different adsorption behavior, which in turn affects the ability of a material to catalyze reactions [15–17], to act as a gas sensor [18–20], or to be functionalized with various molecules [21,22]. The shape of a particle also plays a role in tuning material properties such as ferromagnetism [23–25] or cellular internalization [26]. Therefore, it is the combination of nanoparticle composition, size, surfaces, and shape that ultimately defines their properties.

A notorious issue with producing nanoparticles is reproducibly controlling their shape and size. There are two ways one can handle this issue scientifically. The first is to deal with producing the material as a nucleation and growth problem. In the thermodynamic limit, what should be produced is the thermodynamic Wulff shape [27–29]. With step-flow growth in the kinetic limit, the kinetic Wulff shape should be produced [30,31]. Other cases, such as when diffusion in the fluid during growth is rate-limited [32–34], are also well established. With estimates or measurements of terms such as activation energy barriers, one can predict how to control the particle shape and size. However, in many cases, particularly for solution-based growth, the product is often more empirical, and a second approach is used; one iteratively varies parameters with some informed knowledge to produce the desired shape. In the contemporary literature, this has led to approaches that frequently work, but

success is not guaranteed. There are advantages to approaching the problem as one of nucleation and growth instead. In a recent analysis of the growth of KTaO_3 nanoparticles [35], it was determined that the growth process could be subdivided into two regimes, one with a high chemical potential difference where terrace nucleation and rough-stepped surfaces dominated, and one with a lower chemical potential difference where step-flow growth annihilated steps to smooth surfaces. This analysis leads to predictions regarding which parameters need to be varied to control the nucleation and growth processes, ultimately tuning the conditions to produce particles with specific shapes or sizes.

Our target materials here are the rare-earth scandates (REScO_3), which can adopt a wide range of lattice parameters by varying the rare earth [36]. Only the larger rare-earth elements ($\text{RE} = \text{La-Dy}$) form in the perovskite phase with scandium, whereas the bixbyite structure is formed with the smaller rare-earth elements ($\text{RE} = \text{Y, Ho-Lu}$) [37–39]. LuScO_3 , for example, has only formed the perovskite phase when epitaxially stabilized on a NdGaO_3 or DyScO_3 substrate [40]. As these materials have mostly been used as dielectrics [41], substrates [36], and recently, flexoelectrics [42], they have often been prepared as thin films by atomic layer deposition [43] or pulsed laser deposition [44,45], or as single crystals using the Czochralski technique [36]. Using these materials in applications that require high surface area powders, such as heterogeneous catalysis [46] or gas capture [47] and separation [48], requires a different approach. Unfortunately, there are currently no reports of any solvothermal synthesis of REScO_3 , likely owing to the negligible solubilities of the basic large rare-earth oxides in the alkaline conditions typically used to produce oxide nanoparticles [49].

We recently reported that high surface area GdScO_3 particles could be produced at $300\text{ }^\circ\text{C}$ through the decomposition of a mixed-cation hydroxide hydrogel in a humid environment within a sealed autoclave [50], but the method was not able to produce particles with a controlled size, surface structure, or morphology. The intention of this note is to provide specific information on a two-step approach where we have successfully exploited nucleation and growth to produce well-faceted particles of rare-earth scandates by first using a higher temperature in a furnace with better control of the humidity to nucleate the relevant oxide, then a lower temperature to control step-flow growth to smooth the surface. We suggest that this is a route towards consistent and reproducible production of shape-controlled nanoparticles that we argue is quite general.

2. Materials and Methods

Faceted REScO_3 nanoparticles were produced as follows. First, a rare-earth nitrate precursor was prepared by dissolving 4 mmol of RE_2O_3 ($\text{RE} = \text{La, Nd, Sm, Gd}$) and Sc_2O_3 in 20 mL of 15.8 N nitric acid maintained at $80\text{ }^\circ\text{C}$ until the liquid evaporated. The nitrate precursor was then dissolved in 20 mL of deionized water and added dropwise to 50 mL of 10 M NaOH to precipitate a gel. This gel was cleaned several times by rinsing with deionized water and centrifuged before being transferred to an alumina boat and then to a tube furnace. Argon gas was flowed through a bubbler filled with deionized water placed upstream to create a humid growth environment. The water vapor pressure after the bubbler was estimated to be 23.4 mbar, assuming complete saturation of the Ar flow at room temperature. For completeness, we note that compared to prior work in autoclaves, the chemical potential of the water vapor was better controlled because the humidity was decreased and more consistent using the bubbler and tube furnace. The gel was either subjected to a one-step heat treatment at a temperature between 200 and $450\text{ }^\circ\text{C}$ for 2 days to determine the optimum reaction conditions, or a two-step heat treatment with a high-temperature step at $450\text{ }^\circ\text{C}$ for 2 days followed by a low-temperature step at $300\text{ }^\circ\text{C}$ for 1 day, to produce faceted nanoparticles. Based upon the results of the one-step heat treatments, these temperatures were identified as appropriate for nucleation ($450\text{ }^\circ\text{C}$) and surface smoothing ($300\text{ }^\circ\text{C}$), respectively. The final products were rinsed with deionized water and centrifuged several times, then put into an oven at $80\text{ }^\circ\text{C}$ to dry overnight.

Powder X-ray diffraction (PXRD) was performed on a Rigaku Ultima diffractometer (Rigaku Corporation, Tokyo, Japan) using a $\text{Cu K}\alpha$ source operated at 40 kV and 44 mA. Secondary electron (SE) imaging was performed on a Hitachi HD-2300 (Hitachi, Ltd., Tokyo, Japan) scanning transmission

electron microscope operated at 200 kV. For completeness, we note that the SE images did not show the surfaces of these materials as clearly as with other oxides, owing to the long mean-free path of the low-energy secondary electrons and the near co-incidence of the vacuum level and band gap as discussed elsewhere [42]. High-resolution electron microscopy (HREM) was performed on a JEOL ARM300F GrandARM S/TEM (JEOL, Ltd., Tokyo, Japan) operated at 300 kV.

3. Results

Figure 1 shows PXRD patterns of the GdScO_3 nanoparticles produced using a single temperature between 200 and 450 °C for 2 days in a humid environment. At 200 °C, only $\text{Gd}(\text{OH})_3$ was formed. At 250 and 300 °C, GdScO_3 was the primary phase, but GdOOH was also present. At higher temperatures, the product was nearly entirely GdScO_3 , with a minimal amount of Gd_2O_3 . The morphology of GdScO_3 particles produced at different temperatures was studied using SE imaging (Figure 2). The lower temperature conditions yielded large particles with evident faceting. In contrast, at higher temperatures, the perovskite particles were smaller in size and had less-defined faceting. Scherrer analysis of the X-ray diffraction patterns indicated that the average particle size decreased with increasing reaction temperature; average particle sizes of 93.4(7) nm, 58.5(4) nm, and 51.0(4) nm were calculated for particles produced at 350, 400, and 450 °C, respectively.

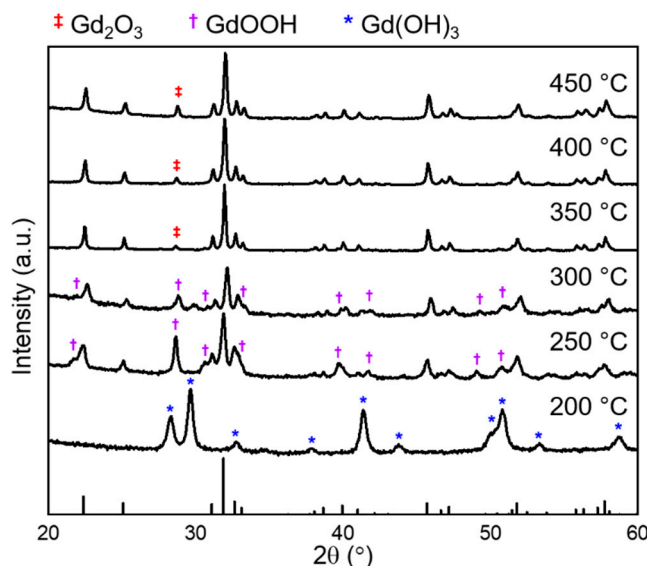


Figure 1. PXRD patterns of the products obtained from reaction attempts of GdScO_3 at a single temperature between 200 and 450 °C for 2 days. The calculated pattern for GdScO_3 is plotted on the bottom. $\text{Gd}(\text{OH})_3$ (blue *) was the only crystalline product formed at 200 °C, implying that ΔG_{rxn} , as defined later in the text, is positive. Between 250 and 300 °C, both GdScO_3 and GdOOH (purple †) are formed, suggesting ΔG_{rxn} is negative but small in absolute value. Above 300 °C, GdScO_3 is the primary phase, with only a small amount of Gd_2O_3 (red †) as a secondary phase, so ΔG_{rxn} is negative and large in absolute value.

A two-step heat treatment (450 °C for 2 days, followed by 300 °C for 1 day) was performed for several REScO_3 (RE = La, Nd, Sm, Gd). Only the larger RE elements were investigated, because only they react to form the perovskite phase. In fact, an attempt to make LuScO_3 only produced a solid solution in the bixbyite structure, as expected [37–39]. PXRD patterns of the REScO_3 (RE = La, Nd, Sm, Gd) (Figure 3) confirmed that perovskite REScO_3 was the primary phase, with minimal amounts of $\text{RE}(\text{OH})_3$ and/or RE_2O_3 as secondary phases. The perovskite particles were faceted as shown in the SE images of Figure 4; an example HREM image and corresponding power spectrum of a NdScO_3 particle in Figure 5 show that the particles were primarily pseudo-cubic {100}- and {110}-terminated.

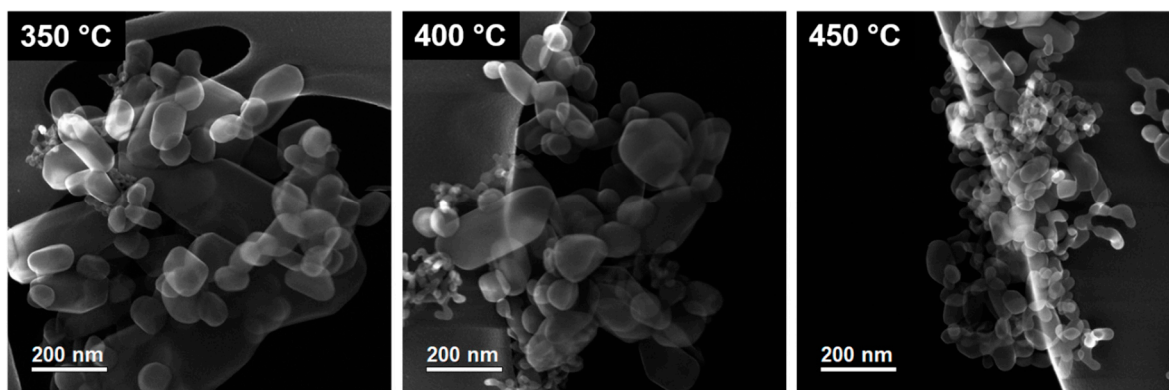


Figure 2. SE images of GdScO_3 produced at 350, 400, and 450 °C. GdScO_3 grown at lower temperatures had a less negative ΔG_{rxn} and consequently had more faceting and were larger than particles grown at higher temperatures (see later discussion). Note that SE images do not show the surfaces of GdScO_3 as clearly as other oxides do, as discussed in the text.

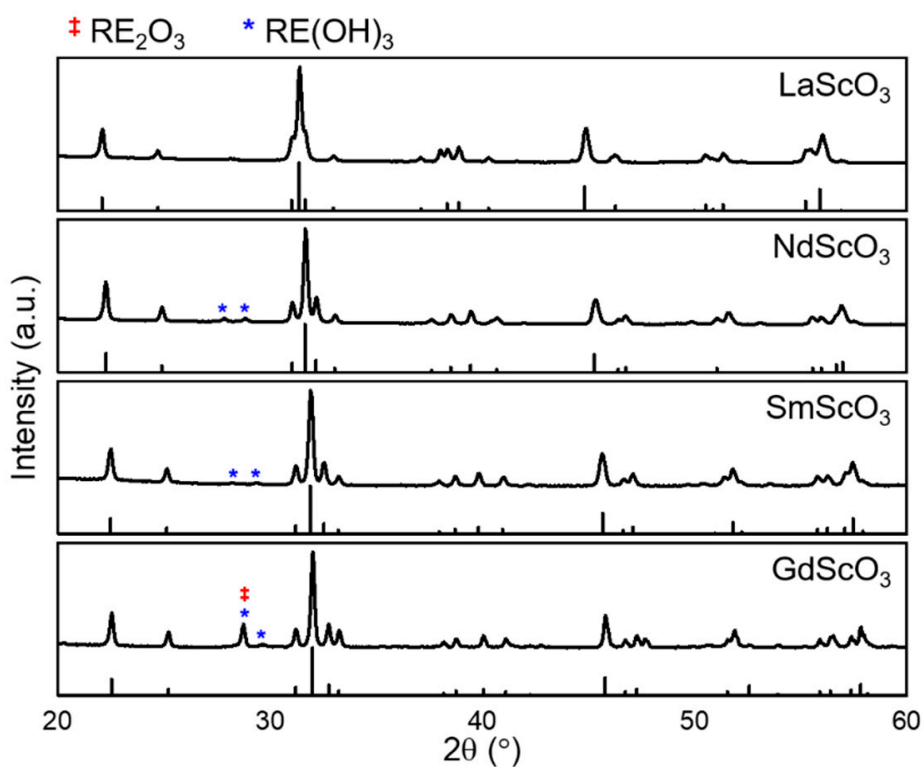


Figure 3. PXRD patterns of REScO_3 (RE = La, Nd, Sm, Gd) particles obtained using the two-step heat treatment at 450 °C for 2 days and then 300 °C for 1 day. The calculated patterns for the corresponding REScO_3 are plotted below. The perovskite phase was the primary product, with trace RE(OH)_3 (blue *) or RE_2O_3 (red †) as secondary products.

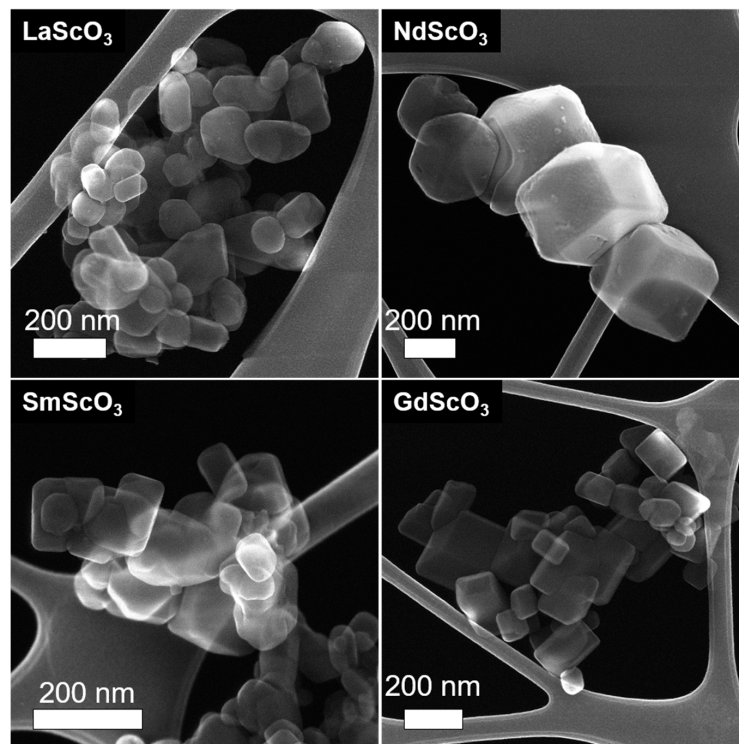


Figure 4. SE images of REScO_3 (RE = La, Nd, Sm, Gd) produced using the two-step heat treatment at 450 °C for 2 days and then 300 °C for 1 day. Smaller particles were produced because the high-temperature step had a more negative ΔG_{rxn} , which led to a higher nucleation rate. The particles are more faceted because the low-temperature step had a less negative ΔG_{rxn} , so step-flow terrace growth dominated. Note that SE images do not show the surfaces of REScO_3 as clearly as other oxides do, as discussed in the text.

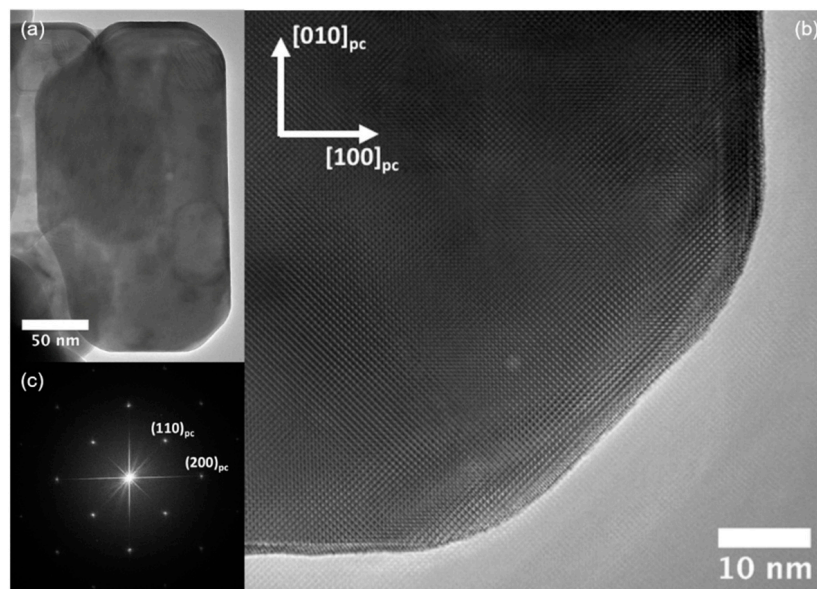
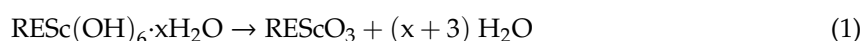


Figure 5. (a) Low magnification HREM image of a faceted NdScO_3 particle produced using the two-step heat treatment at 450 °C for 2 days and then 300 °C for 1 day. (b) Enlarged HREM image of the lower-right corner of the nanoparticle. (c) Corresponding power spectrum of the entire particle indexed to show that it is terminated with the pseudo-cubic $\{100\}$ and $\{110\}$ surfaces.

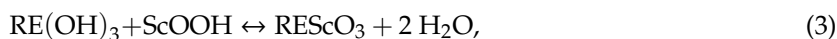
4. Discussion

The results illustrate an approach where higher temperatures are exploited for nucleation, and lower temperatures for growing well-faceted nanoparticles. We will begin by discussing the reaction from the rare-earth hydroxide hydrogel to the perovskite RE₂ScO₇, then the approach to size and shape control.

Our previous report [50] on the formation of crystalline GdScO₃ from a mixed-cation hydroxide hydrogel in a water vapor-assisted reaction [51] noted the role that the humid conditions played in both preserving an open gel matrix and providing the necessary diffusion for the reactions that produced the perovskite, as insufficient diffusion instead produced an amorphous xerogel. Based on the observed products, there were two competing reactions at play:



Reaction (1) accounts for the formation of our desired products (the perovskite phase and water), whereas reaction (2) produces undesired phases which may be in the form of rare-earth oxides, hydroxides, or oxide hydroxides. Equivalently, this competition can be represented by the following reaction:



In reaction (3), the non-standard state Gibbs free energy change of reaction (ΔG_{rxn}) is the difference between the non-standard state Gibbs free energy change of reaction of the desired products (the perovskite phase and water) vs that of the possible undesired products (rare-earth oxides, hydroxides, or oxide hydroxides). When ΔG_{rxn} is negative, the perovskite phase and water will form; when positive, the rare-earth oxides, hydroxides, or oxide hydroxides. Increasing the amount of water will increase ΔG_{rxn} and lead to the formation of the rare-earth hydroxides. In the previous work, the gel was heated in a sealed autoclave, where increases in temperature also increased the pressure. However, temperature and pressure affect the chemical potential of the water vapor in opposite ways—higher temperatures decrease the chemical potential, whereas higher pressures increase the chemical potential—which confounds good experimental control. Under such conditions, the increasing temperature increases the vapor pressure of the water, and while the increase in temperature decreases the chemical potential of the water because of the greater entropic contribution of the water vapor, the increase in pressure increases the chemical potential because of the greater work done by the water vapor. In the work herein, the pressure does not change, so the consequences of increasing the temperature are much more predictable.

PXRD studies (Figure 1) of the products at various temperatures provided insight into the ΔG_{rxn} of forming GdScO₃ from the mixed cation hydroxide gel. Below 250 °C, ΔG_{rxn} was positive so GdScO₃ was not formed. Between 250 and 300 °C, GdScO₃ began to form, suggesting that ΔG_{rxn} was negative but close to zero in this temperature range. With increasing temperature, ΔG_{rxn} became increasingly more negative, which increased the driving force to forming GdScO₃. We note that the identity of the non-perovskite phase changed as a function of temperature. At 200 °C, when no perovskite was produced, the phase that was formed was Gd(OH)₃. Between 250 and 300 °C, where the perovskite phase began forming, the other phase was GdOOH rather than Gd(OH)₃. At higher temperatures still, the secondary phase was Gd₂O₃. This increased dehydration from Gd(OH)₃ to GdOOH to Gd₂O₃ was expected with increasing temperature because of the substantial entropy of gaseous H₂O. The fact that the onset of forming the perovskite phase correlated with the onset of GdOOH may imply that the dehydration from Gd(OH)₃ to GdOOH was a necessary step for subsequent reaction into GdScO₃. We note that the ancillary evidence supports the hypothesis that the formation of REOOH is a necessary step for the hydrothermal synthesis of REMnO₃ [52]. However, the formation of REOOH was not observed with LaScO₃, NdScO₃, and SmScO₃, where RE(OH)₃ was the only other identified secondary

phase. The possibility of REOOH rehydrating into RE(OH)₃ upon cooling could not be discounted and requires in situ experiments to investigate further.

Turning to the particle shape, in addition to the phase, the dominant nucleation and growth mechanisms also evolved with changes in ΔG_{rxn} . The three key components are (1) particle nucleation, where a small particle is nucleated from the gel, (2) terrace nucleation, where new terraces are nucleated atop existing terraces, and (3) terrace growth, where existing terraces on the particle surface grow laterally until they reach the edge of the particle and are annihilated, leading to smooth facets. While all three mechanisms occur, it is the mechanism with the highest rate that will determine the final shape and size. When ΔG_{rxn} is positive, the desired reaction to produce the perovskite does not occur. When ΔG_{rxn} is negative but small, the reaction occurs with a relatively small driving force and growth processes due to heterogeneous nucleation, such as terrace nucleation and terrace growth, are favored so large particles with smooth surfaces are formed. With an increasingly negative ΔG_{rxn} , the driving force of the reaction increases such that processes due to homogeneous nucleation can occur more readily, which leads to a high particle nucleation rate and consequently small particles. Between the two growth mechanisms, terrace nucleation has a higher rate than terrace growth, so the particle surfaces are rougher. These understandings agree well with the particle size and morphology observed through the SE imaging (Figure 2) of GdScO₃ produced at various temperatures. At lower temperatures, where ΔG_{rxn} was small and negative, terrace nucleation and growth dominated, which led to the formation of larger particles with smoother facets. With increasing temperature, ΔG_{rxn} became increasingly more negative, such that particle nucleation dominated and produced more particles that were smaller and had less well-defined surfaces and morphology. Scherrer analysis of the X-ray diffraction patterns indicated that the average particle size decreased with increasing reaction temperature, as predicted. At the lower temperatures, nucleation of the rare-earth scandates can proceed over an extended time, which will lead to a distribution of sizes; the small GdScO₃ particulates also observed in Figure 2 reflect this.

Two different sequential reaction conditions are necessary for better-faceted and smaller nanoparticles: a step with a large negative ΔG_{rxn} to promote the reaction to the desired product and nucleate many small but rough particles with high surface area, followed by a step with a small negative ΔG_{rxn} to promote terrace growth that smooths the surfaces leading to well-defined facets. For this particular reaction, meeting these conditions involved a high-temperature nucleation step followed by a low-temperature smoothing step. Temperatures of 450 and 300 °C were chosen for nucleation and smoothing, based on the one-step heat treatment results. SE imaging of REScO₃ (RE = La, Nd, Sm, Gd) particles (Figure 4) confirmed that these conditions led to smaller and better faceted particles, as the GdScO₃ particles produced with the two-step heat treatment (Figure 4) were more faceted than those produced with only a single nucleation step (Figure 2). Increasing the nucleation temperature further would likely increase the nucleation rate and reduce particle size [35]. In addition, the small particulates found in the one-step samples were no longer present in the two-step heat treatment. This follows expectations; at the lower temperature of the second step, homogeneous nucleation of new particles will be suppressed, while growth via (slow) nucleation of new terraces on existing particles and (faster) step-flow growth will dominate. NdScO₃, SmScO₃, and GdScO₃ formed particles that were cuboidal in shape, terminated by pseudo-cubic {001} surfaces, with edges truncated by the pseudo-cubic {110} surfaces. Evidence for this can be found in the HREM image and corresponding power spectrum of an NdScO₃ particle in Figure 5. Further analysis of the REScO₃ surface structures is ongoing. LaScO₃ appeared to be less faceted, a difference that may suggest the temperature for terrace growth is lower for LaScO₃ than for the other REScO₃. We hypothesize that a higher yield of particles with strong faceting can be achieved by optimizing the temperature and duration of the nucleation and smoothing steps for each material.

5. Conclusions

A method for producing faceted RE₂ScO₃ nanoparticles based upon a two-step process is described. Higher temperatures are used in the first step to nucleate particles and lower temperatures in the second step to promote surface smoothing. This approach—exploiting the nucleation and growth mechanisms—is not unique to this system, and can be utilized to inform reaction conditions and thereby tailor morphology and surface structure in general.

Author Contributions: Conceptualization, R.J.P., T.L., K.R.P., and L.D.M.; Data curation, R.J.P., T.L., Z.R.M., K.R.P., and L.D.M.; Formal analysis, R.J.P.; Funding acquisition, K.R.P. and L.D.M.; Investigation, R.J.P., T.L., and Z.R.M.; Methodology, R.J.P. and T.L.; Project administration, K.R.P. and L.D.M.; Resources, K.R.P. and L.D.M.; Supervision, K.R.P. and L.D.M.; Validation, R.J.P., T.L., and Z.R.M.; Visualization, R.J.P., T.L., and Z.R.M.; Writing—original draft, R.J.P.; Writing—review & editing, R.J.P., T.L., Z.R.M., K.R.P., and L.D.M.

Funding: This research was funded by the Northwestern University Institute for Catalysis in Energy Processes (ICEP) on Grant No. DOE DE-FG02-03-ER 15457, which supported R.J.P. and Z.R.M., and the National Science Foundation on Grant No. DMR-1507101, which supported T.L. ICEP is funded by the Chemical Sciences, Geosciences, and Biosciences Division, Office of Science, U.S. Department of Energy.

Conflicts of Interest: The authors declare no conflict of interest.

References

1. Moshfegh, A.Z. Nanoparticle Catalysts. *J. Phys. D Appl. Phys.* **2009**, *42*, 233001. [[CrossRef](#)]
2. Ringe, E.; Sharma, B.; Henry, A.-I.; Marks, L.D.; Van Duyne, R.P. Single Nanoparticle Plasmonics. *Phys. Chem. Chem. Phys.* **2013**, *15*, 4110–4129. [[CrossRef](#)]
3. Raj, S.; Jose, S.; Sumod, U.S.; Sabitha, M. Nanotechnology in Cosmetics: Opportunities and Challenges. *J. Pharm. Bioallied Sci.* **2012**, *4*, 186–193. [[CrossRef](#)]
4. Basak, A.K.; Pramanik, A.; Islam, M.N.; Anandakrishnan, V. Challenges and Recent Developments on Nanoparticle-Reinforced Metal Matrix Composites. In *Fillers and Reinforcements for Advanced Nanocomposites*; Dong, Y., Umer, R., Lau, A.K.-T., Eds.; Woodhead Publishing: Sawston, Cambridge, UK, 2015; pp. 349–367.
5. De Jong, W.H.; Borm, P.J.A. Drug Delivery and Nanoparticles: Applications and Hazards. *Int. J. Nanomed.* **2008**, *3*, 133–149. [[CrossRef](#)]
6. Escudero, A.; Becerro Ana, I.; Carrillo-Carrión, C.; Núñez Nuria, O.; Zyuzin Mikhail, V.; Laguna, M.; González-Mancebo, D.; Ocaña, M.; Parak Wolfgang, J. Rare earth based nanostructured materials: synthesis, functionalization, properties and bioimaging and biosensing applications. *Nanophotonics* **2017**, *6*, 881–921. [[CrossRef](#)]
7. Escudero, A.; Carrillo-Carrión, C.; Zyuzin, M.V.; Parak, W.J. Luminescent Rare-earth-based Nanoparticles: A Summarized Overview of their Synthesis, Functionalization, and Applications. *Top. Curr. Chem.* **2016**, *374*, 48. [[CrossRef](#)] [[PubMed](#)]
8. Roduner, E. Size Matters: Why Nanomaterials Are Different. *Chem. Soc. Rev.* **2006**, *35*, 583–592. [[CrossRef](#)]
9. Smith, A.M.; Nie, S. Semiconductor Nanocrystals: Structure, Properties, and Band Gap Engineering. *Acc. Chem. Res.* **2010**, *43*, 190–200. [[CrossRef](#)]
10. Kelly, K.L.; Coronado, E.; Zhao, L.L.; Schatz, G.C. The Optical Properties of Metal Nanoparticles: The Influence of Size, Shape, and Dielectric Environment. *J. Phys. Chem. B* **2003**, *107*, 668–677. [[CrossRef](#)]
11. Kreibig, U. Electronic Properties of Small Silver Particles: The Optical Constants and Their Temperature Dependence. *J. Phys. F Met. Phys.* **1974**, *4*, 999–1014. [[CrossRef](#)]
12. Varghese, J.; Whatmore, R.W.; Holmes, J.D. Ferroelectric Nanoparticles, Wires and Tubes: Synthesis, Characterisation and Applications. *J. Mater. Chem. C* **2013**, *1*, 2618–2638. [[CrossRef](#)]
13. Ge, H.; Huang, Y.; Hou, Y.; Xiao, H.; Zhu, M. Size Dependence of the Polarization and Dielectric Properties of KNbO₃ Nanoparticles. *RSC Adv.* **2014**, *4*, 23344–23350. [[CrossRef](#)]
14. Cheng, H.; Yang, N.; Lu, Q.; Zhang, Z.; Zhang, H. Syntheses and Properties of Metal Nanomaterials with Novel Crystal Phases. *Adv. Mater.* **2018**, *30*, 1707189. [[CrossRef](#)]
15. Lee, I.; Morales, R.; Albiter, M.A.; Zaera, F. Synthesis of Heterogeneous Catalysts with Well Shaped Platinum Particles to Control Reaction Selectivity. *Proc. Natl. Acad. Sci. USA* **2008**, *105*, 15241–15426. [[CrossRef](#)]

16. Collins, G.; Schmidt, M.; O'Dwyer, C.; Holmes Justin, D.; McClacken Gerard, P. The Origin of Shape Sensitivity in Palladium-Catalyzed Suzuki–Miyaura Cross Coupling Reactions. *Angew. Chem. Int. Ed.* **2014**, *53*, 4142–4145. [[CrossRef](#)]
17. Geng, G.; Chen, P.; Guan, B.; Jiang, L.; Xu, Z.; Di, D.; Tu, Z.; Hao, W.; Yi, Y.; Chen, C.; et al. Shape-Controlled Metal-Free Catalysts: Facet-Sensitive Catalytic Activity Induced by the Arrangement Pattern of Noncovalent Supramolecular Chains. *ACS Nano* **2017**, *11*, 4866–4876. [[CrossRef](#)]
18. Sun, Y.-F.; Liu, S.-B.; Meng, F.-L.; Liu, J.-Y.; Jin, Z.; Kong, L.-T.; Liu, J.-H. Metal Oxide Nanostructures and Their Gas Sensing Properties: A Review. *Sensors* **2012**, *12*, 2610–2631. [[CrossRef](#)]
19. Rao, X.; Su, X.; Yang, C.; Wang, J.; Zhen, X.; Ling, D. From Spindle-Like β -FeOOH Nanoparticles to α -Fe₂O₃ Polyhedral Crystals: Shape Evolution, Growth Mechanism and Gas Sensing Property. *CrystEngComm* **2013**, *15*, 7250–7256. [[CrossRef](#)]
20. Jońca, J.; Ryzhikov, A.; Kahn, M.L.; Fajerweg, K.; Chaudret, B.; Chapelle, A.; Menini, P.; Fau, P. Shape-Controlled ZnO Nanostructures for Gas Sensing Applications. *Procedia Eng.* **2014**, *87*, 907–910. [[CrossRef](#)]
21. Subbiah, R.; Veerapandian, M.; Yun, K.S. Nanoparticles: Functionalization and Multifunctional Applications in Biomedical Sciences. *Curr. Med. Chem.* **2010**, *17*, 4559–4577. [[CrossRef](#)]
22. Mout, R.; Moyano, D.F.; Rana, S.; Rotello, V.M. Surface Functionalization of Nanoparticles for Nanomedicine. *Chem. Soc. Rev.* **2012**, *41*, 2539–2544. [[CrossRef](#)]
23. Kolhatkar, A.G.; Jamison, A.C.; Litvinov, D.; Willson, R.C.; Lee, T.R. Tuning the Magnetic Properties of Nanoparticles. *Int. J. Mol. Sci.* **2013**, *14*, 15977–16009. [[CrossRef](#)]
24. Li, Y.; Li, Y.; Wang, T. The Size and Shape Dependence of Ferromagnetism in Nanomagnets. *J. Nanomater.* **2012**, *2012*, 897023. [[CrossRef](#)]
25. Cao, L.-F.; Xie, D.; Guo, M.-X.; Park, H.S.; Fujita, T. Size and Shape Effects on Curie Temperature of Ferromagnetic Nanoparticles. *Trans. Nonferrous Met. Soc. China* **2007**, *17*, 1451–1455. [[CrossRef](#)]
26. Gratton, S.E.A.; Ropp, P.A.; Pohlhaus, P.D.; Luft, J.C.; Madden, V.J.; Napier, M.E.; DeSimone, J.M. The effect of particle design on cellular internalization pathways. *Proc. Natl. Acad. Sci. USA* **2008**, *105*, 11613–11618. [[CrossRef](#)]
27. Hoffman, D.W.; Cahn, J.W. A Vector Thermodynamics for Anisotropic Surfaces: I. Fundamentals and Application to Plane Surface Junctions. *Surf. Sci.* **1972**, *31*, 368–388. [[CrossRef](#)]
28. Cahn, J.L.; Hoffman, D.L. A Vector Thermodynamics for Anisotropic Surfaces—II. Curved and Faceted Surfaces. *Acta Metall.* **1974**, *22*, 1205–1214. [[CrossRef](#)]
29. Dinghas, A. Über einen geometrischen Satz von Wulff für die Gleichgewichtsform von Kristallen. *Z. Kristallogr. Cryst. Mater.* **1943**, *105*, 304–314. [[CrossRef](#)]
30. Angenent, S.; Gurtin, M.E. Multiphase Thermomechanics with Interfacial Structure 2. Evolution of an Isothermal Interface. *Arch. Ration. Mech. Anal.* **1989**, *108*, 323–391. [[CrossRef](#)]
31. Yokoyama, E.; Sekerka, R.F. A Numerical Study of the Combined Effect of Anisotropic Surface Tension and Interface Kinetics on Pattern Formation during the Growth of Two-Dimensional Crystals. *J. Cryst. Growth* **1992**, *125*, 389–403. [[CrossRef](#)]
32. Berg, W.F. Crystal Growth from Solutions. *Proc. R. Soc. Lond. Ser. A* **1938**, *164*, 79–95.
33. Ham, F.S. Theory of Diffusion-Limited Precipitation. *J. Phys. Chem. Solids* **1958**, *6*, 335–351. [[CrossRef](#)]
34. Burton, W.K.; Cabrera, N.; Frank, F.C. The Growth of Crystals and the Equilibrium Structure of Their Surfaces. *Proc. R. Soc. Lond. Ser. A* **1951**, *243*, 299–358. [[CrossRef](#)]
35. Ly, T.; Wen, J.; Marks, L.D. Kinetic Growth Regimes of Hydrothermally Synthesized Potassium Tantalate Nanoparticles. *Nano Lett.* **2018**, *18*, 5186–5191. [[CrossRef](#)] [[PubMed](#)]
36. Uecker, R.; Velickov, B.; Klimm, D.; Bertram, R.; Bernhagen, M.; Rabe, M.; Albrecht, M.; Fornari, R.; Schlom, D.G. Properties of Rare-Earth Scandate Single Crystals (Re=Nd–Dy). *J. Cryst. Growth* **2008**, *310*, 2649–2658. [[CrossRef](#)]
37. Schneider, S.J.; Roth, R.S.; Waring, J.L. Solid state reactions involving oxides of trivalent cations. *J. Res. Natl. Bur. Stand. A Phys. Chem.* **1961**, *65A*, 345–374. [[CrossRef](#)]
38. Badie, J.M.; Foex, M. Determination experimentale, calcul et prevision de certains diagrammes Sc₂O₃-Ln₂O₃. *J. Solid State Chem.* **1978**, *26*, 311–319. [[CrossRef](#)]
39. Giaquinta, D.M.; zur Loye, H.-C. Structural Predictions in the ABO₃ Phase Diagram. *Chem. Mater.* **1994**, *6*, 365–372. [[CrossRef](#)]

40. Heeg, T.; Roeckerath, M.; Schubert, J.; Zander, W.; Buchal, C.; Chen, H.Y.; Jia, C.L.; Jia, Y.; Adamo, C.; Schlom, D.G. Epitaxially stabilized growth of orthorhombic LuScO₃ thin films. *Appl. Phys. Lett.* **2007**, *90*, 192901. [[CrossRef](#)]
41. Zhao, C.; Witters, T.; Brijs, B.; Bender, H.; Richard, O.; Caymax, M.; Heeg, T.; Schubert, J.; Afanas'ev, V.V.; Stesmans, A.; et al. Ternary Rare-Earth Metal Oxide High-k Layers on Silicon Oxide. *Appl. Phys. Lett.* **2005**, *86*, 132903. [[CrossRef](#)]
42. Koirala, P.; Mizzi, C.A.; Marks, L.D. Direct Observation of Large Flexoelectric Bending at the Nanoscale in Lanthanide Scandates. *Nano Lett.* **2018**, *18*, 3850–3856. [[CrossRef](#)]
43. Myllymaki, P.; Roeckerath, M.; Lopes, J.M.; Schubert, J.; Mizohata, K.; Putkonen, M.; Niinisto, L. Rare Earth Scandate Thin Films by Atomic Layer Deposition: Effect of the Rare Earth Cation Size. *J. Mater. Chem.* **2010**, *20*, 4207–4212. [[CrossRef](#)]
44. Christen, H.M.; Jellison, G.E.; Ohkubo, I.; Huang, S.; Reeves, M.E.; Cicerella, E.; Freeouf, J.L.; Jia, Y.; Schlom, D.G. Dielectric and Optical Properties of Epitaxial Rare-Earth Scandate Films and Their Crystallization Behavior. *Appl. Phys. Lett.* **2006**, *88*, 262906. [[CrossRef](#)]
45. Iacopetti, S.; Shekhter, P.; Winter, R.; Tromm, T.C.U.; Schubert, J.; Eizenberg, M. The Asymmetric Band Structure and Electrical Behavior of the GdScO₃/GaN System. *J. Appl. Phys.* **2017**, *121*, 205303. [[CrossRef](#)]
46. Somorjai, G.A.; Li, Y. *Introduction to Surface Chemistry and Catalysis*; John Wiley & Sons: Hoboken, NJ, USA, 2010.
47. Sanz-Pérez, E.S.; Murdock, C.R.; Didas, S.A.; Jones, C.W. Direct Capture of CO₂ from Ambient Air. *Chem. Rev.* **2016**, *116*, 11840–11876. [[CrossRef](#)]
48. Pozun, Z.D.; Tran, K.; Shi, A.; Smith, R.H.; Henkelman, G. Why Silver Nanoparticles Are Effective for Olefin/Paraffin Separations. *J. Phys. Chem. C* **2011**, *115*, 1811–1818. [[CrossRef](#)]
49. Moeller, T.; Kremers, H.E. The Basicity Characteristics of Scandium, Yttrium, and the Rare Earth Elements. *Chem. Rev.* **1945**, *37*, 97–159. [[CrossRef](#)]
50. Paull, R.J.; Mansley, Z.R.; Ly, T.; Marks, L.D.; Poepelmeier, K.R. Synthesis of Gadolinium Scandate from a Hydroxide Hydrogel. *Inorg. Chem.* **2018**, *57*, 4104–4108. [[CrossRef](#)]
51. Kozawa, T.; Yanagisawa, K.; Suzuki, Y. Water Vapor-Assisted Solid-State Reaction for the Synthesis of Nanocrystalline BaZrO₃ powder. *J. Ceram. Soc. Jpn.* **2013**, *121*, 308–312. [[CrossRef](#)]
52. Stampler, E.S.; Sheets, W.C.; Prellier, W.; Marks, T.J.; Poepelmeier, K.R. Hydrothermal Synthesis of LnMnO₃ (Ln = Ho-Lu and Y): Exploiting Amphoterism in Late Rare-Earth Oxides. *J. Mater. Chem.* **2009**, *19*, 4375–4381. [[CrossRef](#)]



© 2019 by the authors. Licensee MDPI, Basel, Switzerland. This article is an open access article distributed under the terms and conditions of the Creative Commons Attribution (CC BY) license (<http://creativecommons.org/licenses/by/4.0/>).